Clay mineral type and content control properties of fine-grained CO_2 caprocks — Laboratory insights from strongly-swelling and non-swelling clay-quartz mixtures

Mohammad Nooraiepour [1,*]

[1] Department of Geosciences, University of Oslo, P.O. Box 1047 Blindern, 0316 Oslo, Norway

* Correspondence: mohammad.nooraiepour@geo.uio.no

Article

Clay mineral type and content control properties of fine-grained CO_2 caprocks—Laboratory insights from strongly-swelling and non-swelling clay-quartz mixtures

Mohammad Nooraiepour [1,*]

[1] CO_2 Storage Research Group, Department of Geosciences, University of Oslo, P.O. Box 1047 Blindern, 0316 Oslo, Norway
* Correspondence: mohammad.nooraiepour@geo.uio.no

Abstract: Understanding and predicting sealing characteristics and containment efficiency as a function of burial depth across sedimentary basins is a prerequisite for safe and secure subsurface CO_2 storage. Instead of estimators and empirical relationships, this study aims to delineate bounds and variability domains for non-cemented fine-grained sediments. Constant rate of strain uniaxial compression experiments were performed to measure changes in rock properties of brine-saturated quartz-clay mixtures. The binary mixtures were prepared by mixing quartz with strongly-swelling (smectite) and non-swelling (kaolinite) clays representing endmember characteristics within the clay minerals. The primary objective was to evaluate the evolution of mudstone rock properties in the first 2.5 km of burial depth (approximately 25 MPa effective vertical stress) before chemical compaction and cementation. By conducting systematic laboratory tests, variability domains, normal compaction trends, and the boundaries in which characteristics of fine-grained argillaceous CO_2 caprocks may vary were identified and quantified. The results showed distinct property domains for kaolinite-rich and smectite-rich mudstones as endmember mineralogical composition scenarios. In addition, two discrepancies were discovered in the literature and resolved regarding maximum possible compaction and ultimate lowest porosity. The present experimental study can provide inputs for numerical simulation and geological modeling of candidate CO_2 storage sites.

Keywords: Permeability; Porosity; Elastic Moduli; Seismic Properties; Effective Stress; Mechanical Compaction; Mudstone; Caprock; Petrophysics; Rock Physics

1. Introduction

Fine-grained clastic sediments are the most abundant deposits of sedimentary basins and yet among the least investigated sedimentary rocks. Because of the markedly distinct properties of mudstones and shales compared to sandstones, they are of fundamental importance as caprocks for anthropogenic-related storage sites such as geological CO_2 sequestration and waste repositories [1–5], and conventional and unconventional petroleum-related activities [6–8].

Rock properties of the fine-grained argillaceous sediments are strongly affected by local geologic trends. They may markedly change even within a sedimentary basin [4,9–11]. The geological trends can be divided into compaction trends and depositional trends [9,12]. In other words, critical geologic parameters that determine the evolution of rock properties are either related to burial history or depositional environment. Post-depositional processes modify mudstone properties during burial through mechanical and chemical compactions. How depositional trends and lateral variability dictate the changes in macro-scale rock properties should also be incorporated in basin-wide interpretations. Such knowledge and understanding are crucial, particularly in areas with little or no well log information, to constrain geological and geophysical models and reduce uncertainties in predicting rock and fluid properties. This study will focus on sediment burial and compaction trends.

There are two different conceptual models, as presented in Figure 1, which explain the post-depositional changes related to compaction trends in mudstones. These two frameworks define the relative impact and the domain of influence for mechanical and chemical compactions as a function of temperature or burial depth.

The first conceptual model, the left side of Figure 1, states that after the initial mechanical compaction, there is a transition zone during which clay diagenesis, cementation, and chemical compaction begin simultaneously as mechanical compaction is still active [13,14]. At higher temperatures, chemical compaction (cementation) is the only governing mechanism that continues, by implication, independent of the effective stress [13,14]. However, the importance, presence, and span of the transition zone are discussed and highlighted dissimilar in literature proposing the first model (e.g., Bjørlykke in [15]). For instance, Storvoll and Brevik [16] assert that at the onset of chemical compaction, when quartz cement precipitates, the grain contacts become more stable, the stress distributes on a larger surface area because of the cement, and as a result, increase in effective vertical stress becomes insufficient to overcome the strength and stability of the grain framework. They, hence, conclude that it marks the end and stop of mechanical compaction and the beginning of sole chemical compaction [16].

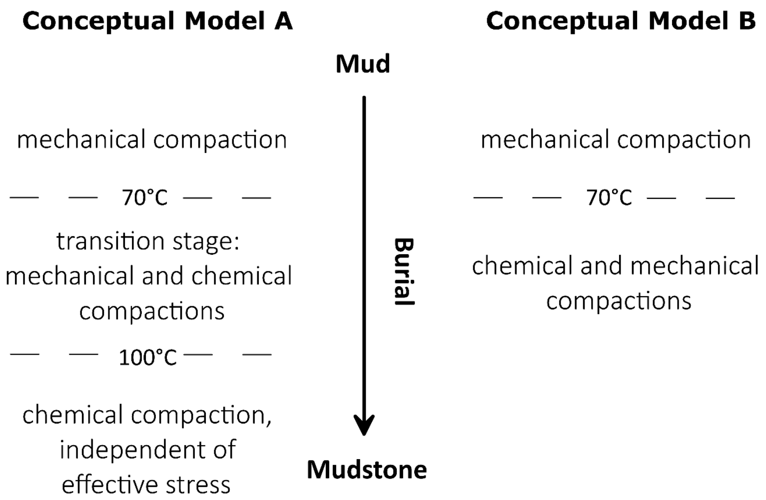

Figure 1. Alternative conceptual models for the relative impact of mechanical and chemical compactions on mudstones during burial (modified from [3,17]).

The right side of Figure 1 presents the second conceptual model. It states that both chemical and mechanical compactions are responsible for the changes in mudstone properties after the onset of clay mineral transformation [17–19]. Moreover, there is no implication in the second model about mechanical compaction getting negligible at temperatures above 100°C. Goulty et al. [19] documented evidence of mechanical compaction in response to increased effective stress up to 130°C.

Another group of scientists, such as Day-Stirrat et al. [20], while using the first conceptual model, have incorporated the second model by stating that there is a mutual impact of mechanical and chemical compactions at deeper depths. Chemical compaction dominates the mutual impact, and the effect of mechanical compaction eventually fades away [20,21]. In which depth or above which temperature interval, the mechanical compaction fades away, and the chemical compaction becomes the only governing factor, however, remain elusive.

In contrast to what is often assumed for mudstones to use a single curve normal compaction trend (NCT), fine-grained argillaceous rocks show a considerable scatter in compaction curves during burial, even in the mechanical compaction domain [3,4,7,11,22–25]. Depending on the microstructure and composition of the constituents in terms of mineralogy and grain size, a boundary or domain should be used to describe mudstone properties instead of a single line or equation. Until recently, though, mudstones and shales have often been considered similar lithology types, and not much attention has been given to the micro-scale properties [6].

The mechanical properties and elastic moduli will increase as a result of increasing effective vertical stress, which in turn leads to an increase in acoustic velocity during burial. The elastic moduli increase rapidly during early compaction, up until 10 MPa, because of the significant porosity loss at low-stress levels. Afterward, they show a steady and gentle increase as the grains get closer and become more densely packed. While these moduli increase monotonically during mechanical compaction with the decrease in porosity or increase of effective vertical stress, they show different behaviors when chemical compaction begins [11,16,26]. In particular, the shear modulus reacts distinctly above and below an apparent knee-point, representing the initiation of quartz cementation. The knee-point is characterized by a sharp increase in shear modulus and change in the trend line.

In the mechanical compaction domain, the Athy-like exponential decline in porosity can generally describe porosity compaction curves [27]. The shape of the compaction curves is controlled by microstructure [25,28,29], which in turn, determines the pore space properties and the available intergranular volume for cementation [21,30]. At the onset of chemical compaction, the precipitated cement does not significantly influence porosity or bulk density because the pore volume only changes slightly [31]. It, however, results in a significant increase in velocity-depth trends [3,32] as incipient quartz cementation near grain contacts causes a rapid and considerable framework stiffening [7,33,34]. Therefore, the early quartz cementation causes a substantial increase in shear modulus. It is why shear wave velocity indicates a much higher sensitivity to weak cementation than compressional wave velocity [16,35]. As burial depth increases and chemical compaction continues, total porosity decreases and acoustic velocity increases. However, it has less impact on the continued stiffening of grain framework and, consequently, elastic moduli [11,16,32].

There are two different approaches to describing the physical properties of rocks, namely, "estimators" and "bounds." In contrast to bounds that provide a range of potential variations in rock properties, given the limited subsurface data that we typically have, the estimators give a specific value for the rock property. For instance, when Archie's Law is being used to predict saturation or Gassmann's equations are being applied to see how effective moduli vary as a function of pore fluid variations. However, rock microstructure and micro-scale properties are controlling factors that determine where the values should locate within the boundaries and why estimators cannot provide a universal solution and may fail or mislead us.

The mechanical compaction experiments in the laboratory provide the opportunity to study the evolution of rock properties during burial and compare the results with in-situ measurements in natural settings. The experiments simulate the compaction of sediments in a normally-compacted basin before the onset of chemical compaction and cementation. The evolution of petrophysical, rock physics, and geomechanical properties of mixtures of quartz-kaolinite and quartz-smectite during laboratory compaction is presented here. The concurrent study of non-swelling (kaolinite) and strongly-swelling (smectite) clay minerals provides insights into the boundaries in which properties of fine-grained sediments and mudstone caprocks may change as a result of burial and increase in effective stress.

2. Materials and Methods

2.1. Sample preparation and characterization

A total of 8 brine-saturated specimens of quartz-clay mixtures were tested. Each specimen was tested twice to ensure repeatability. The synthetic samples were prepared by mixing quartz grains with non-swelling (kaolinite) and strongly-swelling (smectite) clay minerals. The quartz grains are composed of silt-sized (4-63 μm) and very fine sand-sized

(63-125 μm) aggregates. The quartz-clay samples were obtained by mixing quartz with different weight percentages of kaolinite or smectite clay groups. The quartz-clay weight percentages were 85:15, 50:50, 15:85, and 0:100. Therefore, four quartz-clay mixtures were tested for each kaolinite (non-swelling) and smectite (strongly-swelling) clay mineral.

The mineralogical composition, including whole-rock (bulk) and clay minerals, was identified and quantified using the X-ray diffraction (XRD) technique. A laser particle size analyzer (Beckman Coulter LS13 320) provided the grain size. The detailed procedures of sample characterization were given in [4,11].

2.2. Laboratory setup and experimental procedure

Mechanical compaction experiments using a constant rate of strain protocol were carried out to measure the evolution of petrophysical and rock physics properties. An aqueous solution of 0.6 M (35 g/l) sodium chloride (NaCl, EMSURE®) in distilled water was used to prepare the brine-saturated quartz-clay mixtures. Approximately 55 grams of dry aggregates were used to prepare each brine-saturated sample. The brine-saturated samples were tested using a high-stress oedometer equipped with acoustic measurement transducers. The cross-section of the utilized high-stress oedometer and a schematic of the experimental procedure are shown in Figure 2. Constant rate of strain (CRS) uniaxial compression tests were performed to measure the compressibility of the brine-saturated quartz-clay mixtures [36,37]. Aiming to simulate a close to hydrostatic pressure condition, a strain rate of 0.67% per hour was selected, corresponding to an initial deformation of 0.2 mm per hour for an initial sample height of 30 mm. In these experiments, effective vertical stress was increased to 25 MPa. All experiments were performed with drained loading conditions at room temperature of approximately 19-21°C. A detailed description of the experimental setup for compaction experiments is given [11,25].

2.3. Elastic moduli derivation

Through the pulse transmission technique, the travel time of the acoustic signals that passed a sample of known height was measured and converted the travel time to ultrasonic velocity. The dynamic elastic moduli were extracted from the bulk density (ϱ) and ultrasonic wave velocity measurements. The experimental setup was equipped with two piezoelectric transducers with a resonant frequency of 500 kHz to generate and receive high-quality ultrasonic signals. The pulse transmission technique was used to measure compressional (Vp) and shear wave (Vs) velocities. A detailed derivation of physical properties during compaction experiments is given [11,25].

2.4. Vertical permeability measurement

The constant rate of strain (CRS) compaction technique offers a direct method for computing vertical hydraulic conductivity continuously during the test. Figure 2 demonstrates the applied stress and drainage condition for the performed uniaxial CRS compaction experiment. While the non-moving pedestal was kept undrained, the moving piston allowed the pore fluid to drain to atmospheric pressure (Fig. 2). The procedures given in [36,37] were followed to calculate the vertical permeability of the samples. The permeability values were computed continuously at 5 min time intervals during the compaction experiments. Each specimen was also subjected to several single-phase flow direct permeability measurements to ensure the reliability of the CRS-driven permeability curves. Steady-state flow-through experiments were performed to measure absolute permeability at a constant pressure gradient condition and calculated vertical permeability using Darcy's law [25,38,39].

The vertical permeability measurements were conducted under controlled axial stress and pore pressure. While the oedometer cell was placed on the hydraulic load frame, a computer-controlled screw pump (GDS pressure-volume controller) regulated the vertical stress over the oedometer's top piston using the load frame.

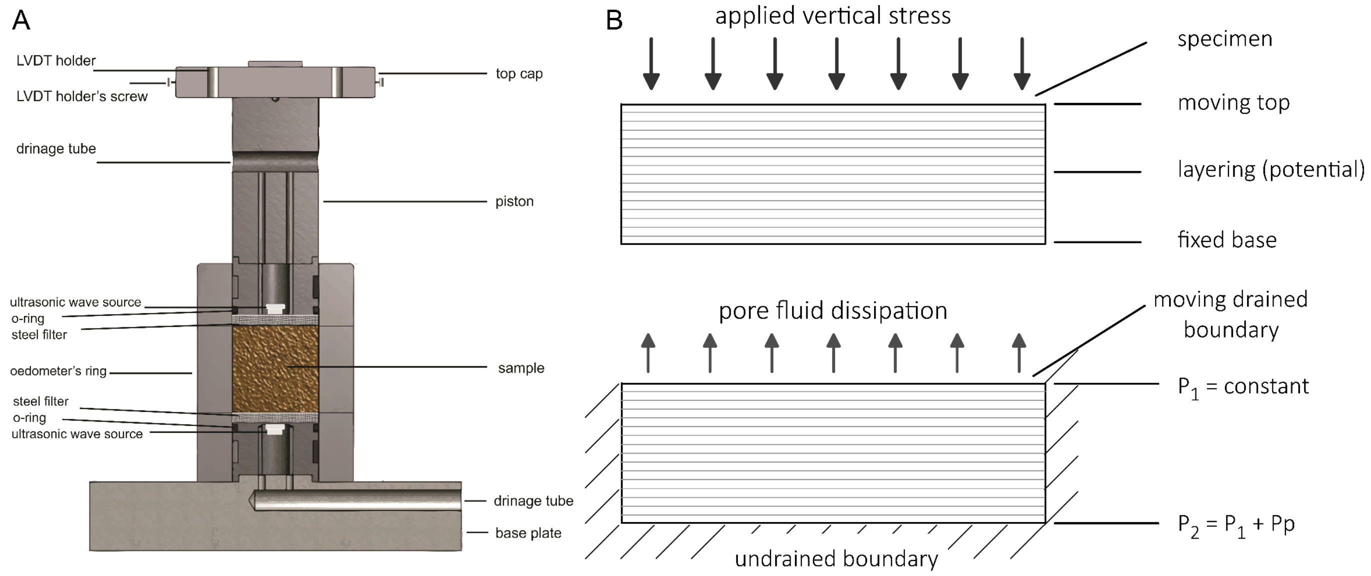

Figure 2. (**a**) A schematic representation of high-stress oedometer compression setup equipped with piezoelectric transducers for real-time Vp and Vs measurements. (**b**) Applied vertical stress and pore fluid drainage conditions during the constant rate of strain (CRS) uniaxial compaction experiments.

Another computer-controlled GDS pump injected the brine at a constant pressure condition via the bottom compartment of the oedometer (inlet). During the permeability test, the pore pressure sensor continuously monitored the lower pore pressure. The top drainage opening (outlet) was connected to a graduated pipette at atmospheric pressure (Poutlet = 0.101 MPa) to collect and measure the displaced pore fluid. To begin with the permeability measurement, the inlet pressure was adjusted to the desired pressure using the inlet GDS controller, and then the inlet valve was opened for flow. Although reaching steady-state flow requires prolonged testing time, the flow rates were only considered for evaluation of vertical permeability once the steady-state flow conditions were achieved.

3. Results and Discussion

In the following sections, the results of laboratory experiments to evaluate the evolution of mudstone rock properties in the first 2.5 km of burial depth (until approximately 25 MPa effective stress) are presented and discussed. Instead of individual compaction curves, the focus is on boundaries and domains in which properties of non-swelling (kaolinite) and strongly-swelling (smectite) clay-rich caprock layers change.

3.1. Changes in rock properties as a function of effective stress

The uniaxial mechanical compaction results of brine-saturated clay-quartz aggregates are presented in Figure 3, where total porosity [%], vertical permeability [mD], compressional wave velocity (Vp) [m/s], and shear wave velocity (Vs) [m/s] are plotted as a function of effective vertical stress [MPa]. The variability domain of kaolinite-rich and smectite-rich mudstone samples are color-coded in violet and green, respectively.

Figure 3 shows a distinct compaction behavior for porosity, permeability, Vp and Vs of quartz-kaolinite and quartz-smectite mixtures. As Figure 3a shows smectite-rich mixtures are less prone to compaction (lower degree of compressibility) than the kaolinite-rich mixtures, with a final total porosity ranging 28-42% and 19-30%, respectively. Therefore, the laboratory compaction results document a wide range of potential values (19-42%, with a span of 23%) for the total porosity of mudstones and fine-grained sediments at the end of the mechanical compaction domain (Fig. 1). Two to three orders of magnitude reduction in vertical permeability were recorded between 1 and 25 MPa effective vertical stresses (Fig. 3b).

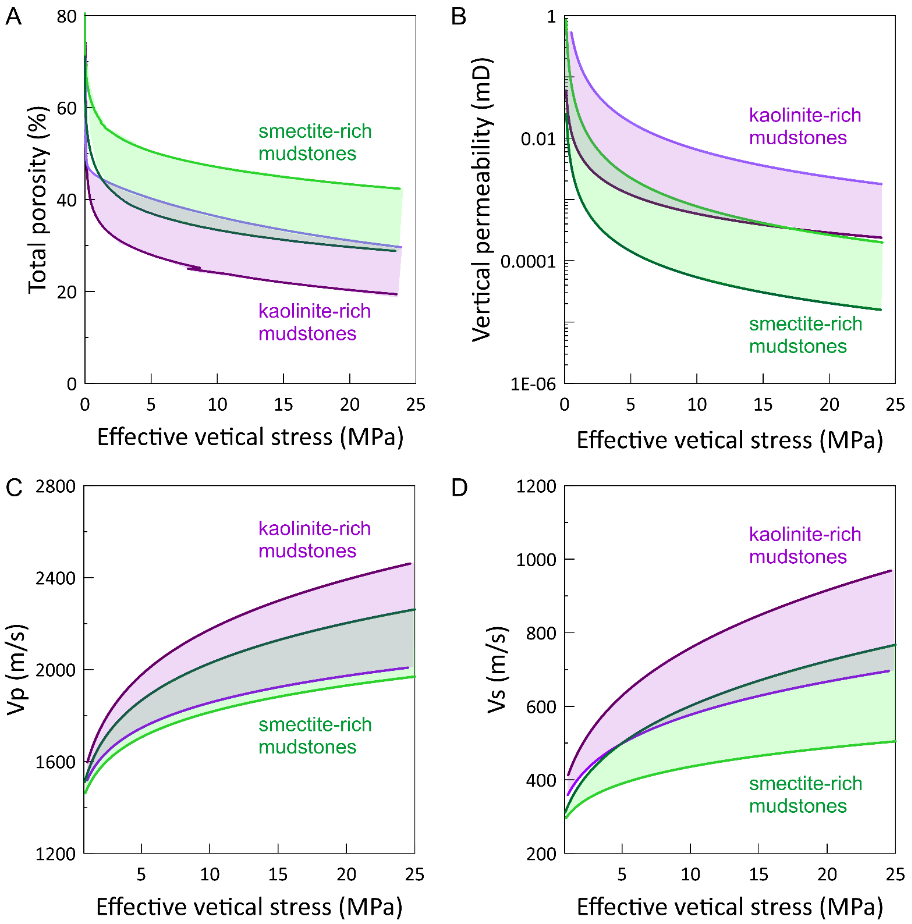

Figure 3. Experimental compaction results of brine-saturated binary quartz-clay mixtures. The evolution of (**a**) total porosity [%], (**b**) vertical permeability [mD], (**c**) compressional wave velocity (Vp) [m/s], and (**d**) shear wave velocity (Vs) [m/s] are plotted as a function of effective vertical stress [MPa]. The variability domain of kaolinite-rich and smectite-rich mudstone samples are color-coded in violet and green, respectively.

The vertical permeability results show approximately two orders of magnitude domain of variability (Fig. 3b). The kaolinite-rich samples show higher permeability (transmissivity) in a range of (≈ 0.001-0.0002 mD) compared to smectite-rich samples (≈ 0.0001-0.00001 mD). Kaolinite-rich fine-grained mixtures consistently show higher Vp and Vs values than smectite-rich specimens (Fig. 3c-d). While compressional wave velocity (Vp) graphs show considerable overlap, the shear wave velocities (Vs) are more or less spanning over two distinct regions with a slight overlap in values. In each subplot in Figure 3, although the tested clay-quartz mixtures have a domain of variability at any given effective stress, the loading curves of the brine-saturated samples are similar in shape, and consequently, the type of mathematical equation that may be used to describe or estimate them.

In Figure 3a, three stages of porosity loss can be identified in the normal compaction trends (NCTs) of fine-grained sediments at a given interval of effective vertical stress, namely I) 0-1 MPa, II) 1-5 MPa, and III) 5-25 MPa effective vertical stress. At stage I, around 40% of initial porosity loss occurs due to the slurry's water loss before grains come in contact at very low effective stresses (up to 1 MPa). A rapid porosity reduction is observable at the early stages of compaction (lower than 10 MPa or approximately the first 1 km burial depth). Stage II (1-5 MPa) defines the shape and susceptibility to loss of the pore volume. Relatively slow and steady compaction occurred between 10 and 25 MPa in stage III. The compaction in this interval is mainly associated with rearrangement, reorientation, and closer packing of the grains. Therefore, similar to Velde's results [28], an exponential and a linear sub-stage can be considered for the mechanically dominated compaction. Careful observation of compaction curves (particularly Fig. 3a) shows that porosity loss before 5 MPa is different for each mixture. The compressibility in this interval defines the form of compaction baseline for each tested sample. This specific compressibility could be related to the development of depositional fabric and the packing of the grains in this interval.

The ultrasonic wave velocity (Vp and Vs) depends considerably on effective vertical stress (Fig. 3c-d). Rapid development in velocity, especially in Vp, is observable in early compaction stages (I-II). As mentioned above, the rapid velocity increase corresponds to the significant porosity loss at low stress levels. The domain of variability in acoustic velocity (both Vp and Vs) increases with the increase in effective vertical stress, and hence during burial in the mechanical compaction domain (Fig. 1). The increment of compressional wave velocity in stage III is nearly the same for all tested samples.

3.2 Changes in rock properties as a function of total porosity

Figure 4 shows the semi-logarithmic cross-plot of vertical permeability (kv) and linear plots of Vp and Vs as a function of measured total porosity (φ). It presents domains of variation in permeability and acoustic wave velocity of endmember quartz-clay mixtures rich in kaolinite (color-coded in violet) and smectite (color-coded in green) clay minerals.

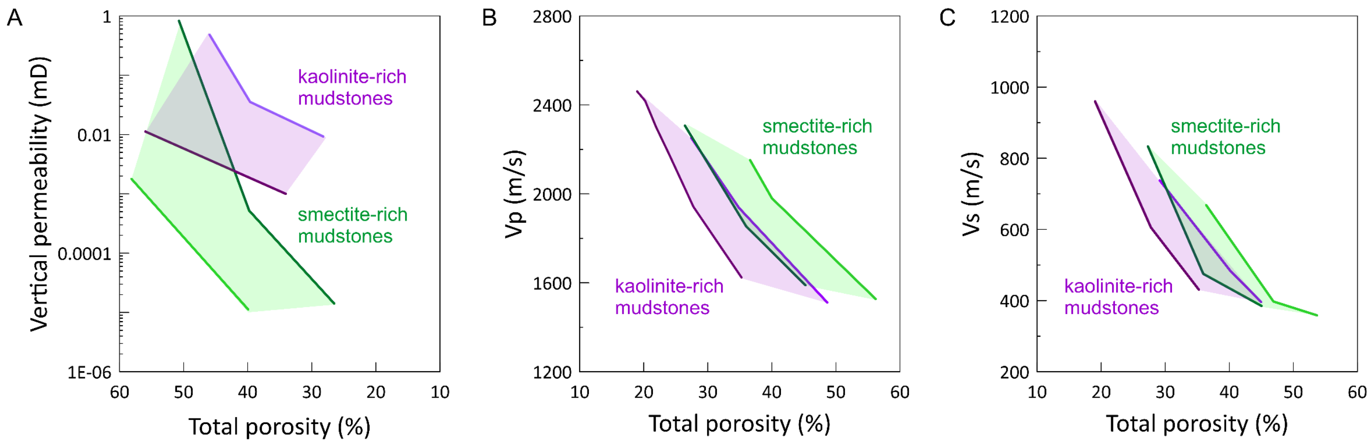

Figure 4. Experimental compaction results of brine-saturated binary quartz-clay mixtures. The evolution (**a**) vertical permeability [mD] in semi-logarithmic plane, (**b**) compressional wave velocity (Vp) [m/s], and (**c**) shear wave velocity (Vs) [m/s] in linear coordinates are plotted as a function of total porosity [%]. The variability domain of kaolinite-rich and smectite-rich mudstone samples are color-coded in violet and green, respectively.

In Figure 4a, the semi-logarithmic (logarithmic ordinate versus linear abscissa) kv-φ relationship indicates that the permeability decline is much faster than the porosity loss and the decrease in permeability is more rapid at higher porosities. Approximately four to five orders of magnitude dispersion between the two boundaries (lowest and highest boundaries of kv-φ relationship) indicate the potential variability of fluid flow properties in fine-grained sediments and mudstones within the mechanical compaction domain.

In analyzing the fluid flow measurements, a negative correlation between the vertical permeability and the content of clay-sized fractions and a positive correlation with the silt-sized particles were identified, consistent with the published literature [e.g., 24,28,38,39]. Although several studies (for instance, Yang and Aplin [42]) proposed that samples with similar content of clay-sized particles show the same permeability, the results of the present study suggest that it is not a universally accurate observation (Figs. 3-3). To be precise, the quartz-clay mudstones show an overall decrease in permeability with the increase of clay-sized content. The relationship, however, is not one-to-one. In other words, a higher clay-sized content does not necessarily mean a lower permeability. It implies that the best-possible packing of different size classes produces the most low-permeability porous medium. The synthetic quartz-clay mixtures range between 10^{-2} and 10^{-5}

mD (Fig. 7). At effective vertical stresses equivalent to 2 km burial depth, the highest and lowest permeabilities among binary mixtures are recorded for the quartz-kaolinite 85:15 and quartz-smectite 15:85 (wt %), respectively.

The strongly-swelling clays (smectitic) markedly influence fluid flow properties of fine-grained sediments, which can be associated with the grain size of these clays [43] and the subsequent influence of pore size and pore throat on the permeability (or transmissivity). Moreover, large specific surface area of the smectite clay group (inversely proportional to grain size) can prevent pore fluid from participating in flow and lead the reduced permeability.

At the start of the uniaxial compression experiments (the equivalent of deposition time in the natural setting in sedimentary basins), the properties of brine-saturated fine-grained quartz-clay mixtures are expected to lie on or near the Reuss bound [7,11,44] as long as they are unconsolidated and weak. The increase of effective vertical stress and consequently decrease in total porosity cause steeper increasing permeability and acoustic velocity trajectories. In Figure 4, permeability, P- and S-wave velocity measurements of non-swelling and strongly-swelling clay-quartz samples show somewhat separate and distinctive domains and, therefore, can be used to construct respective rock physics templates.

The ultrasonic velocity measurements (Vp and Vs) show a general trend of increasing velocity with decreasing total porosity, highlighting the significant porosity control on Vp and Vs of mudstone (and shale) sediments during mechanical compaction. The crossplots of Vp-φ and Vs-φ (Fig. 4b-c) suggest that published velocity-porosity empirical relations cannot be used reliably and broadly because approximately 800 m/s in Vp and 400 m/s in Vs are observable at a given total porosity value. The broad domain of variability in Vp and Vs at the same total porosity highlight the importance of factors such as compositional content (mineralogy and grain size), microfabric, and packing. Therefore, it is essential to consider both velocity and porosity measurements for characterizing mechanically compacted formations on well log data. In addition, it is crucial to consider the coupled effect of clay type and clay content on acoustic velocity and porosity (Figs. 3-4).

3.3 Changes in elastic moduli and rock physics properties

Experimental compaction results of computed dynamic elastic moduli of brine-saturated fine-grained quartz-clay mixtures are presented in Figure 5, where the evolution of elastic moduli, namely, bulk modulus, shear modulus, and Poisson's ratio, are plotted against (top row) effective vertical stress and (bottom row) total porosity. The variability domain of kaolinite-rich and smectite-rich mudstone samples are color-coded in violet and green, respectively.

The cross-plots of elastic moduli demonstrate that the mechanical rock properties of clay-rich sediments strongly depend on the type of clays besides their content, particularly endmembers clay minerals of non-swelling (kaolinite) and strongly-swelling (smectite) nature. A rapid increase in bulk modulus is observable in the early compaction stages (I-II) (Fig. 5a). The rapid increase is attributed to the significant porosity loss at low-stress levels as the bulk modulus indicates how incompressible the samples are. The compressibility rate decreases after 10 MPa effective vertical stress, and the bulk modulus continues to increase almost linearly afterward.

The shear modulus or rigidity indicates a steady and gentle increase during mechanical compaction. The Poisson's ratio shows a considerable drop throughout the experiments. The decline is notable in the first 10 MPa effective vertical stress (Fig. 5c). When specimens resemble incredibly soft water-saturated sediments or suspension of particles in a fluid, the values of Poisson's ratio are around 0.45 and approaching 0.5. The Poisson's ratio experiences an instant fall as effective vertical stress increases. It decreases with a gentler slope toward the end of the tests.

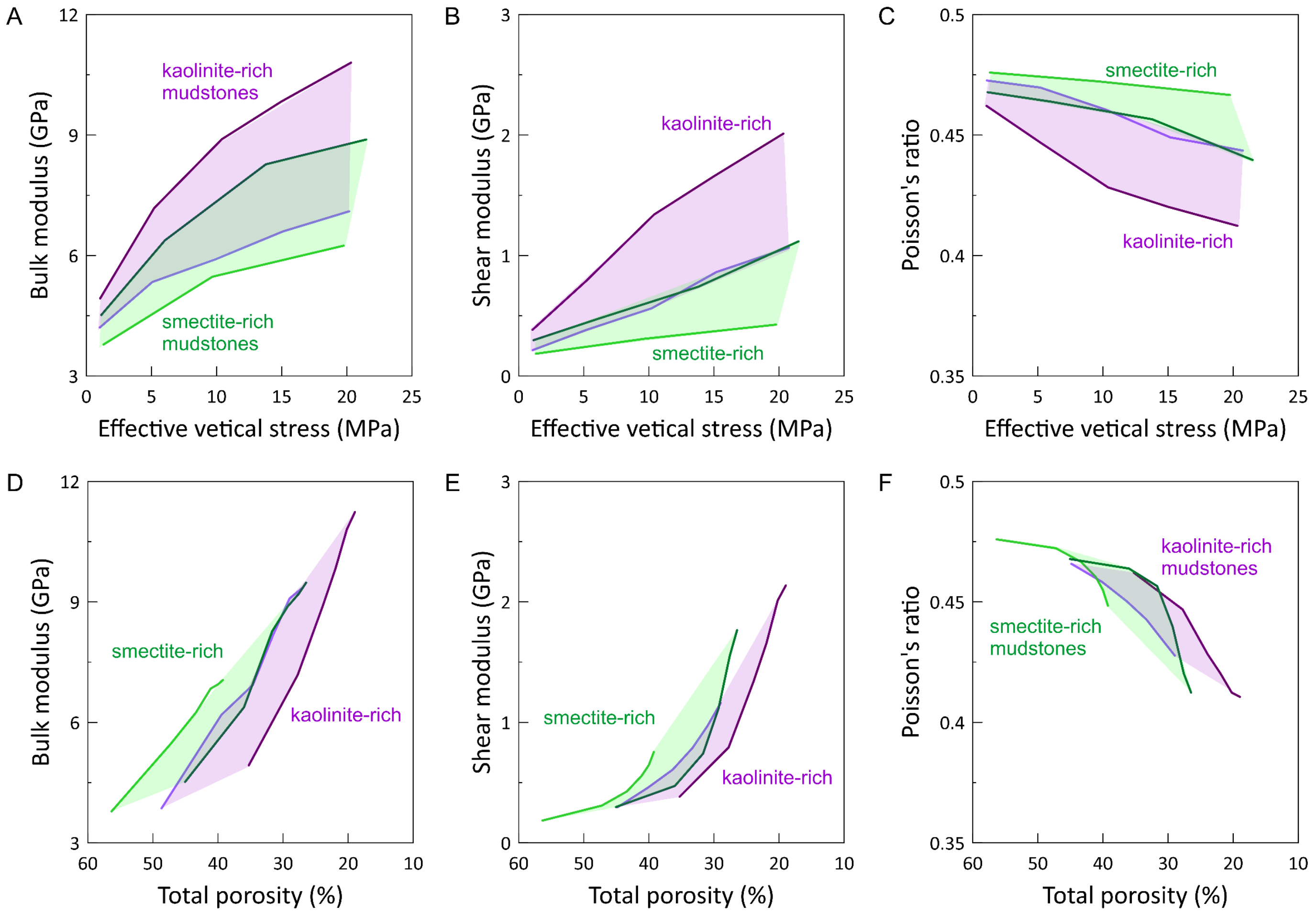

Figure 5. Computed dynamic elastic moduli of brine-saturated binary quartz-clay mixtures. The evolution of elastic moduli, namely, (**a, d**) bulk modulus [GPa], (**b, e**) shear modulus [GPa], and (**c, f**) Poisson's ratio are plotted against (top row) effective vertical stress [MPa] and (bottom row) total porosity [%]. The variability domain of kaolinite-rich and smectite-rich mudstone samples are color-coded in violet and green, respectively.

The scatter in mechanical properties (i.e., elastic moduli) of the tested samples is relatively small at early stress levels, but it increases with effective vertical stress (Fig. 5).

The quartz-kaolinite mixtures have higher bulk and shear moduli and lower Poisson's ratios than the quartz-smectite samples. For the synthetic quartz-clay mixtures (Fig. 4), the endpoint values at 25 MPa effective vertical stress vary approximately in the following ranges: bulk modulus 6.2–11.2 GPa, shear modulus 0.45–2.1 GPa, and Poisson's ratio 0.41–0.46. As end members clay minerals with respect to grain size and surface area, the kaolinite-rich and smectite-rich domains of variability demonstrate the maximum and minimum compressibility (Fig. 5). The smectite-rich samples show notably low rigidity (shear modulus) and Poisson's ratios. The smectite content within the fine-grained sediments is also important because it can cause abnormal pore pressure within the sedimentary strata.

However, regarding the smectite clay fractions, it should be noted that these strongly-swelling fractions constitute a large group of 2:1 (tetrahedral-octahedral-tetrahedral) clay minerals, characterized by low layer charge (0.2–0.6 per half unit cell) and hydrated exchangeable cations [43,45]. These characteristics determine the weakness of linkage between the different layers of a given particle [43,45,46]. Therefore, chemical and structural heterogeneity are typical for species in the smectite group. Both composition and structure are subject to continual variations in time and sedimentary environment [47,48]. The shape of smectites also varies according to the conditions of formation. Species in this group can be found in flakes, curls, and laths of different sizes [43,48]. Also,

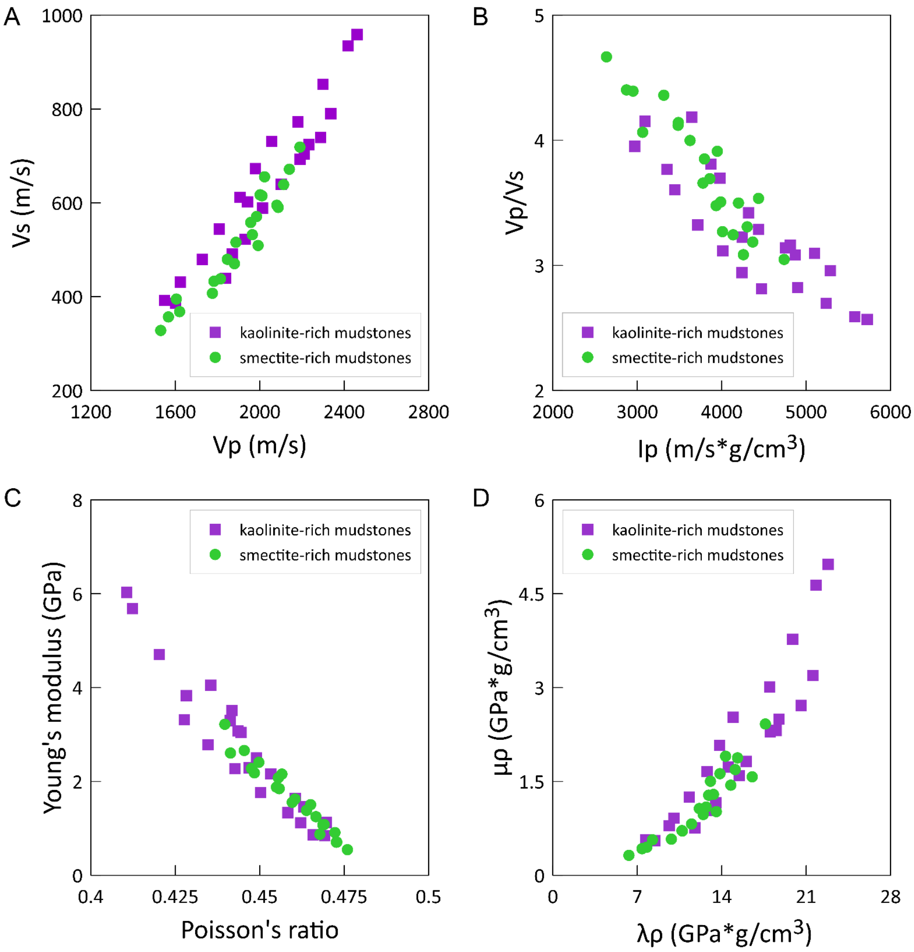

Figure 6. Rock physics crossplots of (**a**) Vp versus Vs, (**b**) Vp/Vs ratio versus acoustic impedance (Ip, P-impedance), (**c**) Young's modulus versus Poisson's ratio; (**d**) μϱ (rigidity times bulk density) versus λϱ (incompressibility times bulk density). Computed and measured properties for kaolinite-rich (squares color-coded in violet) and smectite-rich (circles color-coded in green) clay minerals are shown**.**

smectites are known to be of polydispersive size distribution, which also changes as a result of physical processes and chemical and structural transformations [45,46,48]. Therefore, it is expected that the mechanical properties of species in the smectite group differ significantly from each other.

Figure 6 presents crossplots of a) Vp versus Vs, b) Vp/Vs ratio versus acoustic impedance (Ip, P-impedance), c) Young's modulus versus Poisson's ratio; (d) μϱ (rigidity times bulk density) versus λϱ (incompressibility times bulk density). Computed and measured properties for kaolinite-rich (squares color-coded in violet) and smectite-rich (circles color-coded in green) clay minerals are shown.

As rock physics subplots of Figure 6 show properties of mudstones rich in varying percentages of endmember clay minerals spread over a wide range. Although overlap zones are evident in each crossplot, one can identify that smectite-rich and kaolinite-rich fine-grained sediments have distinctive characteristics. Binary mixtures of quartz-smectite (compared to kaolinite-rich mudstones) show lower Vp and Vs (Fig. 6a), higher Vp/Vs ratio and lower Ip (Fig. 6b), lower Young's modulus and higher Poisson's ratio (Fig. 6c), and finally lower μϱ and λϱ (Fig. 6d). The following intervals of properties are distinctive of brine-saturated kaolinite-rich samples in the mechanical compaction domain: Vp > 2200 m/s, Vs > 750 m/s, Vp/Vs ratio < 3, Ip > 4750, Poisson's ratio > 0.4375, Young's modulus > 3.25, μϱ > 2.5, and λϱ > 17.5 (Fig. 6). Similarly, a specific domain can be identified for smectite-rich samples, owing to their characteristic high total porosity and low shear wave velocity.

3.4 Inconsistencies in the published maximum normal compaction trends (NCTs)

Some discrepancies were found in the literature in assessing the compaction behavior of brine-saturated pure kaolinite clays. As Figure 7 demonstrates, the majority of published kaolinite compaction curves document 17–25% total porosity at 50 MPa effective vertical stress [22,25,49–57]. The coarser kaolinite grains were more susceptible to compaction (more compressible) than the finer size kaolinites. The composite mixture of size classes (as a whole) experienced the most porosity reduction [51]. In contrast, a minority group of literature has reported an entirely different ultimate compaction endpoint, with 11% total porosity at 50 MPa effective vertical stress for brine-saturated kaolinite (Fig. 7). In the present study, two different samples of pure kaolinite powder were purchased and tested to evaluate compaction behavior and endpoint total porosity of kaolinites. The two samples were produced by I) IMERYS, UK (SPES white sort), and II) Potterycraft Ltd., UK. The grain size analyses of purchased kaolinite samples showed mixed class sizes, and therefore, the highest degree of compaction was expected from our experiments. Both kaolinite samples followed similar NCTs and showed approximately 20% final total porosity at 50 MPa effective vertical stress (Fig. 7). Therefore, our laboratory results only confirm the former group of scientists (the majority) and indicate that the 11% value may not be entirely precise.

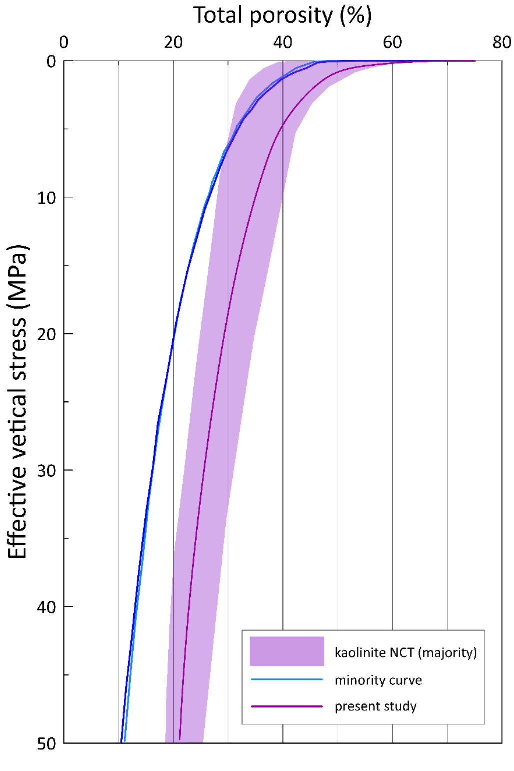

Figure 7. Comparison of published experimental normal compaction trends (NCTs) for brine-saturated pure kaolinite samples. Citations are given in the text.

The second inconsistency was found in recognizing maximum compaction in argillaceous deposits. A group of experimental studies showed that the highest compaction level and maximum porosity loss could be identified for brine-saturated quartz-clay mixtures with 20–40% kaolinite content (and 60-80% quartz) [25,49,53,58–64]. These experimental works have reported a total porosity of around 12% at 50 MPa effective vertical stress for such mixtures. On the other hand, a group of laboratory efforts documented the lowest attainable total porosity at 50 MPa for pure kaolinite samples (φ = 11%). Unexpectedly, the latter group reported that binary mixtures of kaolinite-quartz are less prone to compaction than pure kaolinite. Their experiments showed the most efficient packing (lowest ultimate total porosity for a binary mixture) for the 50:50 kaolinite-quartz with 16% total porosity at 50 MPa effective vertical stress. Our compaction experiments contradict the latter group's claim that the highest compaction is associated with pure kaolinite and confirms that only the best packing of kaolinite-quartz mixture may show the lowest attainable total porosity or highest compressibility [65]. Interestingly enough, the reported porosity value for 50:50 kaolinite-quartz mixture by the second group holds, based on our experiments.

A closer look into the literature supporting second cases in the two aforementioned inconsistencies led to an unexecuted observation. A well-cited group in 2007 reported 11% total porosity at 50 MPa for brine-saturated pure kaolinite, in 2008 19-23%, and in 2009 switched back to 11%. Such discrepancies from a single group without any clarification or comparison with literature bring us to the conclusion that the 11% result for kaolinite's NCT may not be entirely precise and reliable.

4. Concluding Remarks: Implications for top seal integrity

Fluid flow through the rock matrix, pre-existing and induced fracture networks, fault systems, and the geomechanical and geochemical factors associated with CO_2 injection define a caprock layer's sealing capacity and integrity. Fine-grained argillaceous rocks (e.g., mudstones and shales) and evaporates (e.g., salts and anhydrite) are the commonly identified caprocks for CO_2 storage reservoirs [66,67]. Because of their pore space characteristics, these sedimentary sequences effectively act as top sealing sequences in seep and shallow subsurface storages [1,68]. Moreover, fine-grained argillaceous rocks have a profound significance for studying geological processes, geoengineering applications, and conventional and unconventional petroleum-related activities.

Unlike chemical compaction and cementation, which are more challenging to replicate in a laboratory, experimental mechanical compaction of brine-saturated samples enables researchers to study the evolution of mudstone properties as a function of effective vertical stress. The present study investigated variations in physical, hydraulic and acoustic properties of brine-saturated binary clay-quartz mixtures as a function of effective vertical stress. The experiments can simulate the mechanical compaction of sediments in subsiding sedimentary basins with no superimposed tectonic forces before the onset of chemical compaction and cementation. As shown in our previous works [4,11,25], the laboratory results are comparable with in-situ well log measurements in the first 2.5 km burial depth to further investigate rock physics, geomechanics, and compaction-exhumation history of the caprock sequences.

Uniaxial compaction experiments were performed to evaluate the properties of the semi-compacted CO2 seal sequence. It can, however, be expected that the laboratory specimens show reduced anisotropy compared to the natural setting because the aggregates do not settle into layers in the same way as natural deposits do [69,70]. The structures of marine sequences might show a significant degree of anisotropy, which is developed during deposition, compaction, and subsequent straining during burial [71–73]. In addition, it is probable that the clay fractions do not settle with a matching orientation in the laboratory as they become deposited and preferentially oriented in nature. Development of high overpressures, undrained loading, calibration and measurement precision, and violation of other guidelines set by ASTM [37] may cause further uncertainties in the results of a CRS test.

Rigid grains like quartz are expected to withstand the applied stresses and preserve total porosity, while ductile particles like clays bend and block the interparticle pore volumes. The ductile minerals such as clays tend to wrap around the grains at higher stresses, reduce the periphery porosity, and severely impact the permeability [74,75]. Alteration in pore volume during burial may change the pore space connectivity, porous medium morphology, and tortuosity, and therefore, changes in fluid flow and solute transport. The ductile clay fractions in the fine-grained caprocks may also cover reactive solid surfaces, which leads to limited diffusion in the porous layers around the grains and hence, limited (geo)chemical reactions [2]. This armoring phenomenon caused by clay minerals reshapes the available surface area for precipitation and dissolution (geo)chemical reactions during coupled thermo-hydro-mechanical-chemical (THMC) processes, leading to changes in the system's reactivity and reaction progress and rates [2,76–78].

It is generally assumed that the higher the content of clay minerals, the lower the permeability. However, laboratory permeability measurements of the quartz-clay mixtures in this study suggest that the clay type, grain mixing ratio, packing, and potentially preferred orientation of grains must be considered. It is shown that synthetic mixtures of quartz-kaolinite 50:50 and quartz-smectite 15:85 (wt%) give the endmember low permeability among the kaolinite- and smectite-rich mixtures, and therefore, corresponding mudstones rich in non-swelling and strongly-swelling clays.

The presented results indicate that grain size distribution and mineralogical composition are the controlling factors in the porosity-permeability relationships of mudstones and fine-grained clay-rich (argillaceous) subsurface layers. Porosity-permeability relationships are widely proposed to describe the single-phase permeability of mudstones and shales because porosity is a routine and usually available measurement (core analysis and in situ well log measurements). The empirical relationships are typically developed from laboratory measurements (e.g., Yang and Aplin [42]), theoretical models such as the Kozeny-Carman equation (e.g., Chapuis and Aubertin [79]) and the Hagen–Poiseuille equation (e.g., Civan et al. [80]), or binary mixing models (e.g., Revil and Cathles [81]). These approaches often make one or several macroscale assumptions for correlating the total porosity to matrix permeability via applying a tuning factor related to mineralogy, clay fractions, or clay surface area. The present experimental results indicate that seeking to approximate the vertical permeability of fine-grained sediments and mudstones with a single macroscale equation may not provide a universal solution because multiple parameters with not a one-to-one correspondence affect flow characteristics. Incorporating microstructure characteristics of mudstones into the permeability models and considering boundaries (domain of potential variability) instead of single estimators are two necessary directions for subsurface studies. Microstructure characteristics are essential because they control the macroscale fluid flow and transport properties.

Funding: This publication has been produced with support from the project "solid and salt precipitation kinetics during CO_2 injection into reservoir" (SaltPreCO2), funded by the EEA and Norway Grants, Norwegian Financial Mechanism 2014-2021, (UMO-2019/34/H/ST10/00564) through the GRIEG Program, operated by the Polish National Science Centre (NCN) in cooperation with the Research Council of Norway (NFR).

Data Availability Statement: The data and materials that support the findings of this study are available from the corresponding author upon reasonable request.

Acknowledgments: M.N. acknowledges the Faculty of Mathematics and Natural Sciences at University of Oslo (UiO) for granting the Kristine Bonnevie scholarship. The author expresses his gratitude towards Adamson's Foundation in support of geological research, Reusch's grant to promote geography and geology, and Orlaug L. Merkesdal's grant (UiO's Foundation for Funds and Scholarships, UNIFOR).

Conflicts of Interest: The authors declare no competing financial or non-financial interests.

References

1. Song, J.; Zhang, D. Comprehensive review of caprock-sealing mechanisms for geologic carbon sequestration. *Env. Sci Technol* **2013**, *47*, 9–22, doi:10.1021/es301610p.
2. Fazeli, H.; Nooraiepour, M.; Hellevang, H. Microfluidic Study of Fracture Dissolution in Carbonate-Rich Caprocks Subjected to CO2-Charged Brine. *Ind. Eng. Chem. Res.* **2020**, *59*, doi:10.1021/acs.iecr.9b06048.
3. Nooraiepour, M. Rock properties and sealing efficiency in fne-grained siliciclastic caprocks — Implications for CCS and petroleum industry, University of Oslo: Oslo, Norway, 2018, Vol. PhD.
4. Nooraiepour, M.; Haile, B.G.; Hellevang, H. Compaction and mechanical strength of Middle Miocene mudstones in the Norwegian North Sea – The major seal for the Skade CO2 storage reservoir. *Int. J. Greenh. Gas Control* **2017**, *67*, doi:10.1016/j.ijggc.2017.10.016.
5. Nooraiepour, M.; Fazeli, H.; Miri, R.; Hellevang, H. Effect of CO2 Phase States and Flow Rate on Salt Precipitation in Shale Caprocks - A Microfluidic Study. *Environ. Sci. Technol.* **2018**, *52*, 6050–6060, doi:10.1021/acs.est.8b00251.
6. Avseth, P.; Draege, A.; van Wijingaarden, A.J.; Johansen, T.A.; Jørstad, A. Shale rock physics and implications for AVO analysis: A North Sea demonstration. *Lead. Edge (Tulsa, OK)* **2008**, *27*, 788–797, doi:10.1190/1.2944163.
7. Avseth, P.; Mukerji, T.; Mavko, G.; Dvorkin, J. Rock-physics diagnostics of depositional texture, diagenetic alterations, and reservoir heterogeneity in high-porosity siliciclastic sediments and rocks - A review of selected models and suggested work flows. *Geophysics* **2010**, *75*, X75A31-75A47, doi:10.1190/1.3483770.
8. Aplin, A.C.A.C.; Macquaker, J.H.S.J.H.S.J.H.S. Mudstone diversity: Origin and implications for source, seal, and reservoir properties in petroleum systems. *Am. Assoc. Pet. Geol. Bull.* **2011**, *95*, 2031–2059, doi:10.1306/03281110162.
9. Avseth, P.; Flesche, H.; Van Wijngaarden, A.J. AVO classification of lithology and pore fluids constrained by rock physics depth trends. *Lead. Edge (Tulsa, OK)* **2003**, *22*, 1004–1011, doi:10.1190/1.1623641.
10. Loseth, H.; Wensaas, L.; Gading, M.; Duffaut, K.; Springer, M. Can hydrocarbon source rocks be identified on seismic data? *Geology* **2011**, *39*, 1167–1170, doi:10.1130/g32328.1.
11. Nooraiepour, M.; Mondol, N.H.N.H.; Hellevang, H.; Bjørlykke, K. Experimental mechanical compaction of reconstituted shale and mudstone aggregates: Investigation of petrophysical and acoustic properties of SW Barents Sea cap rock sequences. *Mar. Pet. Geol.* **2017**, *80*, 265–292, doi:10.1016/j.marpetgeo.2016.12.003.
12. Haile, B.G.; Klausen, T.G.; Czarniecka, U.; Xi, K.; Jahren, J.; Hellevang, H. How are diagenesis and reservoir quality linked to depositional facies? A deltaic succession, Edgeøya, Svalbard. *Mar. Pet. Geol.* **2018**, *92*, 519–546, doi:10.1016/j.marpetgeo.2017.11.019.
13. Bjørlykke, K.; Høeg, K. Effects of burial diagenesis on stresses, compaction and fluid flow in sedimentary basins. *Mar. Pet. Geol.* **1997**, *14*, 267–276, doi:10.1016/S0264-8172(96)00051-7.
14. Bjørlykke, K. Clay mineral diagenesis in sedimentary basins - A key to the prediction of rock properties. Examples from the North Sea Basin. *Clay Miner.* **1998**, *33*, 14–34.
15. Bjørlykke, K. Compaction of sedimentary rocks: Shales, sandstones and carbonates. In *Petroleum Geoscience: From Sedimentary Environments to Rock Physics, Second Edition*; 2015; pp. 351–360 ISBN 9783642341328.
16. Storvoll, V.; Brevik, I. Identifying time, temperature, and mineralogical effects on chemical compaction in shales by rock physics relations. *Lead. Edge* **2008**, *27*, 750–756, doi:10.1190/1.2944160.
17. Dutta, N.C. Deepwater geohazard prediction using prestack inversion of large offset P-wave data and rock model. *Lead. Edge (Tulsa, OK)* **2002**, *21*, 193–198, doi:10.1190/1.1452612.
18. Lahann, R. Impact of smectite diagenesis on compaction modeling and compaction equilibrium. *AAPG Mem.* **2004**, 61–72.
19. Goulty, N.R.; Sargent, C.; Andras, P.; Aplin, A.C. Compaction of diagenetically altered mudstones – Part 1: Mechanical and chemical contributions. *Mar. Pet. Geol.* **2016**, *77*, 703–713, doi:10.1016/j.marpetgeo.2016.07.015.

20. Day-Stirrat, R.J.J.; McDonnell, A.; Wood, L.J.J. Diagenetic and Seismic concerns associated with interpretation of deeply buried "mobile shales." *AAPG Mem.* **2010**, 5–27, doi:10.1306/13231306M93730.
21. Milliken, K.L.; Day-Stirrat, R.J. Cementation in mudrocksz: Brief review with examples from cratonic basin mudrocks. *AAPG Mem.* **2013**, 133–150, doi:10.1306/13401729H5252.
22. Chilingarian, G. V; Rieke Iii, H.H.; Donaldson, E.C. Chapter 2 Compaction of argillaceous sediments. *Dev. Pet. Sci.* 1995, *41*, 47–164.
23. Giles, M.R.R.; Indrelid, S.L.L.; James, D.M.D.M.D. *Compaction - the great unknown in basin modelling*; 1998; Vol. 141, pp. 15–43;.
24. Bachrach, R. Mechanical compaction in heterogeneous clastic formations from plastic-poroelastic deformation principles: theory and applications. *Geophys. Prospect.* **2016**, doi:10.1111/1365-2478.12159.
25. Nooraiepour, M.; Mondol, N.H.; Hellevang, H. Permeability and physical properties of semi-compacted fine-grained sediments – A laboratory study to constrain mudstone compaction trends. *Mar. Pet. Geol.* **2019**, doi:10.1016/j.marpetgeo.2019.01.019.
26. Baig, I.; Faleide, J.I.J.I.; Jahren, J.; Mondol, N.H.N.H. Cenozoic exhumation on the southwestern Barents Shelf: Estimates and uncertainties constrained from compaction and thermal maturity analyses. *Mar. Pet. Geol.* **2016**, *73*, 105–130, doi:10.1016/j.marpetgeo.2016.02.024.
27. Athy, L.F. Density, Porosity and Compaction of Sedimentary Rocks. *Am. Assoc. Pet. Geol. Bull.* **1930**, *14*, 1–24.
28. Velde, B. Compaction trends of clay-rich deep sea sediments. *Mar. Geol.* **1996**, *133*, 193–201, doi:10.1016/0025-3227(96)00020-5.
29. Schneider, J.; Flemings, P.B.B.; Day-Stirrat, R.J.J.; Germaine, J.T.T. Insights into pore-scale controls on mudstone permeability through resedimentation experiments. *Geology* **2011**, *39*, 1011–1014, doi:10.1130/g32475.1.
30. Peltonen, C.; Marcussen, Ø.; Bjørlykke, K.; Jahren, J. Clay mineral diagenesis and quartz cementation in mudstones: The effects of smectite to illite reaction on rock properties. *Mar. Pet. Geol.* **2009**, *26*, 887–898, doi:10.1016/j.marpetgeo.2008.01.021.
31. Marcussen, Ø.; Faleide, J.I.; Jahren, J.; Bjørlykke, K. Mudstone compaction curves in basin modelling: a study of Mesozoic and Cenozoic Sediments in the northern North Sea. *Basin Res.* **2010**, *22*, 324–340, doi:10.1111/j.1365-2117.2009.00430.x.
32. Vernik, L.; Nur, A. Petrophysical classification of siliciclastics for lithology and porosity prediction from seismic velocities. *Am. Assoc. Pet. Geol. Bull.* **1992**, *76*, 1295–1309.
33. Winkler, K.W. Contact stiffness in granular porous materials: Comparison between theory and experiment. *Geophys. Res. Lett.* **1983**, *10*, 1073–1076, doi:10.1029/GL010i011p01073.
34. Bernabé, Y.; Fryer, D.T.T.; Hayes, J.A.A. The effect of cement on the strength of granular rocks. *Geophys. Res. Lett.* **1992**, *19*, 1511–1514, doi:10.1029/92GL01288.
35. Han, D.-H.H.; Batzle, M. Velocities of deepwater reservoir sands. *Lead. Edge (Tulsa, OK)* **2006**, *25*, 460–466, doi:10.1190/1.2193222.
36. Wissa, A.E.Z.; Christian, J.T.; Davis, E.H.; Heiberg, S.; WISSA AEZ; CHRISTIAN JT; DAVIS EH; HEIBERG S Consolidation at constant rate of strain. *ASCE J Soil Mech Found Div* **1971**, *97*, p 1393-1413.
37. ASTM Standard Test Method for One-Dimensional Consolidation Properties of Saturated Cohesive Soils Using Controlled-Strain Loading 2006, *D4186-06*.
38. Nooraiepour, M.; Bohloli, B.; Park, J.; Sauvin, G.; Skurtveit, E.; Mondol, N.H.H. Effect of brine-CO2 fracture flow on velocity and electrical resistivity of naturally fractured tight sandstones. *Geophysics* **2018**, *83*, WA37–WA48, doi:10.1190/GEO2017-0077.1.
39. Moghadam, J.N.; Nooraiepour, M.; Hellevang, H.; Mondol, N.H.; Aagaard, P. Relative permeability and residual gaseous CO2 saturation in the Jurassic Brentskardhaugen Bed sandstones, Wilhelmøya Subgroup, western central Spitsbergen, Svalbard. *Nor. J. Geol.* **2019**, *99*, 1–12, doi:10.17850/njg005.

40. Gamage, K.; Screaton, E.; Bekins, B.; Aiello, I. Permeability–porosity relationships of subduction zone sediments. *Mar. Geol.* **2011**, *279*, 19–36, doi:10.1016/j.margeo.2010.10.010.
41. Daigle, H.; Screaton, E.J.J. Evolution of sediment permeability during burial and subduction. *Geofluids* **2015**, *15*, 84–105, doi:10.1111/gfl.12090.
42. Yang, Y.; Aplin, A.C. A permeability–porosity relationship for mudstones. *Mar. Pet. Geol.* **2010**, *27*, 1692–1697, doi:10.1016/j.marpetgeo.2009.07.001.
43. Brigatti, M.F.F.; Galán, E.; Theng, B.K.G.K.G. *Structure and Mineralogy of Clay Minerals*; 2013; Vol. 5, pp. 21–81;.
44. Avseth, P.; Mukerji, T.; Mavko, G. *Quantitative seismic interpretation: Applying rock physics tools to reduce interpretation risk*; 2005; Vol. 9780521816; ISBN 9780511600074.
45. Brigatti, M.F.F.; Galán, E.; Theng, B.K.G.K.G.; Schoonheydt, R.A.; Johnston, C.T.; Bergaya, F. 1 - Clay minerals and their surfaces. In *Surface and Interface Chemistry of Clay Minerals*; Schoonheydt, R., Johnston, C.T., Bergaya, F.B.T.-D. in C.S., Eds.; Elsevier, 2018; Vol. 9, pp. 1–21 ISBN 1572-4352.
46. Bergaya, F.; Lagaly, G. Chapter 1 - General Introduction: Clays, Clay Minerals, and Clay Science. In *Handbook of Clay Science*; Bergaya, F., Lagaly, G.B.T.-D. in C.S., Eds.; Elsevier, 2013; Vol. 5, pp. 1–19 ISBN 1572-4352.
47. Haigh, S.K.; Vardanega, P.J. Fundamental basis of single-point liquid limit measurement approaches. *Appl. Clay Sci.* **2014**, *102*, 8–14, doi:10.1016/j.clay.2014.10.011.
48. Emmerich, K. Chapter 2.13 - Full Characterization of Smectites. In *Handbook of Clay Science*; Bergaya, F., Lagaly, G.B.T.-D. in C.S., Eds.; Elsevier, 2013; Vol. 5, pp. 381–404 ISBN 1572-4352.
49. Beloborodov, R.; Pervukhina, M.; Han, T.; Josh, M. Experimental Characterization of Dielectric Properties in Fluid Saturated Artificial Shales. *Geofluids* **2017**, *2017*, 1019461, doi:10.1155/2017/1019461.
50. Chilingar, G. V; Knight, L. Relationship Between Pressure and Moisture Content of Kaolinite, Illite, and Montmorillonite Clays1. *Am. Assoc. Pet. Geol. Bull.* **1960**, *44*, 101–106, doi:10.1306/0BDA5F81-16BD-11D7-8645000102C1865D.
51. Engelhardt, W. von; Gaida, K.H. Concentration changes of pore solutions during compaction of clay sediments. *J. Sediment. Res.* **1963**, *33*, 919–930, doi:10.2110/33.4.919.
52. BROWN PR COMPACTION OF FINE-GRAINED TERRIGENOUS AND CARBONATE SEDIMENTS. A REVIEW. *Bull. Can. Pet. Geol.* **1969**, *17*, 486–495.
53. Marion, D.; Nur, A.; Yin, H.; Han, D. Compressional velocity and porosity in sand-clay mixtures. *GEOPHYSICS* **1992**, *57*, 554–563, doi:10.1190/1.1443269.
54. Robinet, J.C.; Pakzad, M.; Plas, F. Un modèle rhéologique pour les argiles gonflantes. *Rev. française géotechnique* **1994**, 57–67.
55. Vasseur, G.; Djeran-Maigre, I.; Grunberger, D.; Rousset, G.; Tessier, D.; Velde, B. Evolution of structural and physical parameters of clays during experimental compaction. *Mar. Pet. Geol.* **1995**, *12*, 941–954, doi:10.1016/0264-8172(95)98857-2.
56. Djéran-Maigre, I.; Tessier, D.; Grunberger, D.; Velde, B.; Vasseur, G. Evolution of microstructures and of macroscopic properties of some clays during experimental compaction. *Mar. Pet. Geol.* **1998**, *15*, 109–128, doi:10.1016/S0264-8172(97)00062-7.
57. Beloborodov, R.; Pervukhina, M.; Lebedev, M. Compaction trends of full stiffness tensor and fluid permeability in artificial shales. *Geophys. J. Int.* **2018**, *212*, 1687–1693, doi:10.1093/gji/ggx510.
58. Yin, H. Acoustic velocity and attenuation of rocks: isotropy, intrinsic anisotropy, and stress-induced anisotropy, Stanford University: Stanford, USA, 1992, Vol. Ph.D. thes.
59. Dewhurst, D.N.; Aplin, A.C.; Sarda, J.-P.; Yang, Y. Compaction-driven evolution of porosity and permeability in natural mudstones: An experimental study. *J. Geophys. Res. Solid Earth* **1998**, *103*, 651–661.
60. Revil, A.; Grauls, D.; Brévart, O. Mechanical compaction of sand/clay mixtures. *J. Geophys. Res. Solid Earth* **2002**, *107*, ECV 11-1-ECV 11-15, doi:10.1029/2001jb000318.

61. Pitman, T.D.; Robertson, P.K.; Sego, D.C. Influence of fines on the collapse of loose sands. *Can. Geotech. J.* **1994**, *31*, 728–739, doi:10.1139/t94-084.

62. Thevanayagam, S.; Mohan, S. Intergranular state variables and stress–strain behaviour of silty sands. *Géotechnique* **2000**, *50*, 1–23, doi:10.1680/geot.2000.50.1.1.

63. D. Knoll, M.; Knight, R. Relationships between Dielectric and Hydrogeologic Properties of Sand-Clay Mixtures. **1994**, doi:https://doi.org/10.3997/2214-4609-pdb.300.4.

64. Beloborodov, R.; Pervukhina, M.; Luzin, V.; Delle Piane, C.; Clennell, M.B.; Zandi, S.; Lebedev, M. Compaction of quartz-kaolinite mixtures: The influence of the pore fluid composition on the development of their microstructure and elastic anisotropy. *Mar. Pet. Geol.* **2016**, *78*, 426–438, doi:10.1016/j.marpetgeo.2016.09.030.

65. Glover, P.W.J.; Luo, M. The Porosity and Permeability of Binary Grain Mixtures. *Transp. Porous Media* **2020**, *132*, 1–37, doi:10.1007/s11242-020-01378-0.

66. Michael, K.; Golab, A.; Shulakova, V.; Ennis-King, J.; Allinson, G.; Sharma, S.; Aiken, T. Geological storage of CO2 in saline aquifers—A review of the experience from existing storage operations. *Int. J. Greenh. Gas Control* **2010**, *4*, 659–667, doi:10.1016/j.ijggc.2009.12.011.

67. Liu, F.; Lu, P.; Griffith, C.; Hedges, S.W.; Soong, Y.; Hellevang, H.; Zhu, C. CO2–brine–caprock interaction: Reactivity experiments on Eau Claire shale and a review of relevant literature. *Int. J. Greenh. Gas Control* **2012**, *7*, 153–167, doi:10.1016/j.ijggc.2012.01.012.

68. Mallants, D.; Marivoet, J.; Sillen, X. Performance assessment of the disposal of vitrified high-level waste in a clay layer. *J. Nucl. Mater.* **2001**, *298*, 125–135, doi:10.1016/S0022-3115(01)00577-3.

69. Karstunen, M.; Koskinen, M. Plastic anisotropy of soft reconstituted clays. *Can. Geotech. J.* **2008**, *45*, 314–328, doi:10.1139/T07-073.

70. Yin, Z.-Y.; Hattab, M.; Hicher, P.-Y. Multiscale modeling of a sensitive marine clay. *Int. J. Numer. Anal. Methods Geomech.* **2011**, *35*, 1682–1702, doi:10.1002/nag.977.

71. Burland, J.B. On the compressibility and shear strength of natural clays. *Geotechnique* **1990**, *40*, 329–378, doi:10.1680/geot.1990.40.3.329.

72. Hicher, P.Y.; Wahyudi, H.; Tessier, D. Microstructural analysis of inherent and induced anisotropy in clay. *Mech. Cohesive-Frictional Mater.* **2000**, *5*, 341–371, doi:10.1002/1099-1484(200007)5:5<341::AID-CFM99>3.0.CO;2-C.

73. Wheeler, S.J.S.J.; Näätänen, A.; Karstunen, M.; Lojander, M. An anisotropic elastoplastic model for soft clays. *Can. Geotech. J.* **2003**, *40*, 403–418, doi:10.1139/t02-119.

74. Zhao, H.; Ning, Z.; Zhao, T.; Zhang, R.; Wang, Q. Effects of mineralogy on petrophysical properties and permeability estimation of the Upper Triassic Yanchang tight oil sandstones in Ordos Basin, Northern China. *Fuel* **2016**, *186*, 328–338, doi:10.1016/j.fuel.2016.08.096.

75. Fawad, M.; Mondol, N.H.; Jahren, J.; Bjørlykke, K. Microfabric and rock properties of experimentally compressed silt-clay mixtures. *Mar. Pet. Geol.* **2010**, *27*, 1698–1712, doi:10.1016/j.marpetgeo.2009.10.002.

76. Nooraiepour, M.; Masoudi, M.; Hellevang, H. Probabilistic nucleation governs time, amount, and location of mineral precipitation and geometry evolution in the porous medium. *Sci. Rep.* **2021**, *11*, doi:10.1038/s41598-021-95237-7.

77. Nooraiepour, M.; Masoudi, M.; Shokri, N.; Hellevang, H. Probabilistic Nucleation and Crystal Growth in Porous Medium: New Insights from Calcium Carbonate Precipitation on Primary and Secondary Substrates. *ACS Omega* **2021**, *6*, 28072–28083, doi:10.1021/acsomega.1c04147.

78. Deng, H.; Poonoosamy, J.; Molins, S. A reactive transport modeling perspective on the dynamics of interface-coupled dissolution-precipitation. *Appl. Geochemistry* **2022**, *137*, 105207, doi:https://doi.org/10.1016/j.apgeochem.2022.105207.

79. Chapuis, R.P.; Aubertin, M. On the use of the Kozeny◎Carman equation to predict the hydraulic conductivity of soils. *Can.*

Geotech. J. **2003**, *40*, 616–628, doi:10.1139/t03-013.

80. Civan, F.; Rai, C.S.S.; Sondergeld, C.H.H. Shale-Gas Permeability and Diffusivity Inferred by Improved Formulation of Relevant Retention and Transport Mechanisms. *Transp. Porous Media* **2011**, *86*, 925–944, doi:10.1007/s11242-010-9665-x.
81. Revil, A.; Cathles III, L.M.; Cathles, L.M. Permeability of shaly sands. *Water Resour. Res.* **1999**, *35*, 651–662, doi:10.1029/98wr02700.